Journal of Wind Engineering & Industrial Aerodynamics 237 (2023) 105377

Contents lists available at ScienceDirect

Journal of Wind Engineering & Industrial Aerodynamics

journal homepage: www.elsevier.com/locate/jweia

Performance of the porous disk wind turbine model at a high Reynolds number: Solidity distribution and length scales effects

John W. Kurelek *, Alexander Piqué, Marcus Hultmark

Department of Mechanical and Aerospace Engineering, Princeton University, Princeton, 08540, NJ, USA

ARTICLE INFO

Dataset link: https://doi.org/10.1016/j.jweia.2023.105377

Keywords:
Horizontal axis wind turbine
Porous disk
Actuator disk model
High Reynolds number

ABSTRACT

A new design methodology for porous disk wind turbine modeling is proposed, where a disk is matched to a horizontal axis wind turbine (HAWT) on (i) thrust coefficient, (ii) radial solidity distribution, and (iii) length scale criteria. Three disk designs are tested, allowing for isolation of the effects of each criterion, with performance evaluated through experimental wake comparisons with a model HAWT at a diameter-based Reynolds number of 4×10^6 and free-stream turbulence intensity of 1.2%. Wake velocity measurements reveal excellent agreement on mean profiles in the near wake (as early as $1^1/_2$ diameters downstream) when the rotor's radial solidity distribution is incorporated into the disk design. Higher order velocity statistics can also be matched farther downstream ($3^1/_2$ diameters). To match the higher order moments, the disk must generate near wake turbulence of similar characteristics to the rotor, since this turbulence dominates the development of the wake in a high Reynolds number, low free-stream turbulence environment. This is achieved by the third design criterion, where physical features that match the rotor length scales are incorporated. Thus, including all three criteria in a single porous disk yields a model that performs well at field-relevant Reynolds numbers, is not performance dependent on the free-stream turbulence intensity, and does not require iterative tuning.

1. Introduction

Wind energy is an integral component in the United Nations' plan for net zero greenhouse gas emissions by 2050. Total wind energy capacity has continued to grow year-over-year, with a record 53% increase in 2020 bringing the total worldwide installed capacity to 743 GW (GWEC, 2021). However, forecasts predict a needed total wind energy capacity of 6044 GW by 2050 in order to meet climate targets,[1] which would require installation rates to triple over the next decade. If this growth is to take place, much of it is expected to occur offshore – the compound annual growth rate for offshore wind is predicted to be 31.5% through to 2025, compared to 0.3% for onshore (GWEC, 2021) – where significant wind resources can be accessed by horizontal axis wind turbines that now regularly exceed 200 m in diameter (Soares-Ramos et al., 2020).

The success of the HAWT design is due in large part to it scaling well up to large sizes. However, this leads to significant footprint requirements for offshore wind farms, as HAWT wakes can have significant impact up to 15 diameters downstream (Chamorro and Porté-Agel, 2009), and power generation in turbine arrays is greatly affected by interactions with upstream wakes. Practical limitations, such as available space and cabling costs, inevitably lead to turbines operating in the wakes of others. Turbine spacing at operational offshore sites ranges between 4 and 12 diameters (Barthelmie et al., 2010), which is estimated to cost 10 to 50% in unrealized power generation compared to idealized conditions (Barthelmie et al., 2007; Dahlberg and Thor, 2009; Hansen et al., 2012). This, and other important considerations, such as high dynamic loads leading to accelerated fatigue failures (*e.g.*, Tian et al., 2014), has lead to a wealth of research on wake effects within turbine arrays, including numerous experimental (Markfort et al., 2012; Lebron et al., 2012; Newman et al., 2013; Theunissen et al., 2015; Bossuyt et al., 2017) and numerical studies (Calaf et al., 2010; Yang et al., 2012; Meyers and Meneveau, 2012; De Rijcke et al., 2015; Goit and Meyers, 2015). Common to all of these studies is the use of simplifying turbine models, employed either to reduce the complexity of experimental setups or the computational costs of simulations. The latter is essential in Large Eddy Simulations, where direct modeling of multiple HAWTs at relevant Reynolds numbers remains infeasible (Mehta et al., 2014), and so state-of-the-art code bases use actuator methods for turbine modeling. These methods involve replacing the turbine rotor with local volume forces that extract momentum from the flow, either through a uniformly distributed axial force over a circular area (actuator disk

* Corresponding author.
E-mail address: john.kurelek@princeton.edu (J.W. Kurelek).

[1] According to the International Renewable Energy Agency's *Transforming Energy Scenario* (IRENA, 2020).

https://doi.org/10.1016/j.jweia.2023.105377
Received 5 December 2022; Received in revised form 14 February 2023; Accepted 5 March 2023

method) (*e.g.*, Hansen, 2008), or radially varying lines forces that are rotated (actuator line method) (Sørensen and Shen, 2002).

Of these two methods, the actuator disk has seen the most widespread use (Sanderse et al., 2011), as it requires relatively low computational effort while yielding reasonable wake approximations that have been experimentally validated (*e.g.*, Wu and Porté-Agel, 2011; Aubrun et al., 2013; Lignarolo et al., 2014). Implementing the actuator disk concept in a wind tunnel experiment is straightforward, requiring only the rotor be replaced by a suitable porous disk. A porous disk's near wake contains grid generated turbulence, notably lacking the angular momentum, and tip and hub vortices seen in a typical HAWT near wake (*e.g.*, Zhang et al., 2012; Piqué et al., 2022a). However, in the far wake these features are much less significant due to turbulent diffusion, which is primarily driven by the free-stream turbulence level (Aubrun et al., 2013). Thus, in the far wake, where the flow has become self-similar (Vermeer et al., 2003), the predominant means of turbulence production is through velocity shear (Aubrun et al., 2013), and so a porous disk that produces a matching self-similar velocity profile has been shown to yield an accurate representation of a HAWT far wake (Aubrun et al., 2013; Lignarolo et al., 2014; Camp and Cal, 2016).

The goal, therefore, in implementing a physical or numerical actuator disk is to select a design that produces the self-similar velocity profile of a given turbine, which is most often accomplished by matching the disk's thrust coefficient (and induction factor, by equivalence) to the rotor at a given Reynolds number. However, this criterion yields relatively few design constraints, which has led investigators to test a wide variety of porous disks, including those consisting of metal mesh (Myers and Bahaj, 2010; España et al., 2011; Aubrun et al., 2013; Lignarolo et al., 2014), disks perforated with circular holes or slots (Sforza et al., 1981; Higuchi et al., 1997; Blackmore et al., 2014; Theunissen et al., 2015), and 'hub-and-spoke' designs with radially varying porosity (Camp and Cal, 2016, 2019; Bossuyt et al., 2017). Cross-examining these studies, and others comparing different types of disks (Aubrun et al., 2019; Helvig et al., 2021; Vinnes et al., 2022), it is clear that no one type of disk or set of design parameters has emerged as universally applicable, but rather any type of disk can be made to suit a given turbine through careful, iterative tuning. However, this approach is time consuming and can be infeasible when turbine wake characteristics are not known *a priori*, as is often the case in field operation.

Of further concern is an absence of experimental data for porous disks at high Reynolds numbers, $Re_D > 10^6$, with $Re_D = 3.3 \times 10^5$ from Aubrun et al. (2019) being the highest tested to-date, while simulations have and continue to use the actuator disk method at Reynolds numbers above what has been validated (*e.g.*, Calaf et al., 2010; Yang et al., 2012; Goit and Meyers, 2015). For offshore operation in particular, where Reynolds numbers can exceed 10^8 and free-stream turbulence intensities are typically 6%–8% versus 10%–12% onshore (Barthelmie et al., 2005, 2007), legitimate concerns on the applicability of the actuator disk can be raised. First is the aforementioned lack of experimental porous disk data at high Reynolds number, while a minimum threshold for Reynolds number invariance for HAWTs remains a topic of debate in the literature (Chamorro et al., 2012; Miller et al., 2019). Second, increased levels of free-stream turbulence lead to a more rapid diffusion of HAWT near wake structures (Medici and Alfredsson, 2006; Hattori et al., 2007; Krogstad and Adaramola, 2012; Li et al., 2020), and thus more favorable comparisons with porous disk models (Aubrun et al., 2013). Indeed, the studies of Helvig et al. (2021) and Vinnes et al. (2022) demonstrate the significant challenge of matching HAWT and porous disk wakes at low levels of free-stream turbulence.

The objective of the current investigation is therefore two-fold. First, to develop objective design criteria for porous disks that can be used without *a priori* knowledge of a HAWT's wake characteristics. And second, to test the newly developed design at a high Reynolds number and low levels of free-stream turbulence, since such conditions are relevant to offshore HAWT operation and are predicted to be the most challenging for accurate HAWT wake modeling via the porous disk approach. The former is achieved through the development of a novel porous disk design that is specified to match not only a rotor's thrust coefficient, but also its radial solidity distribution and length scales. The latter is then addressed through testing of a model HAWT and porous disks in a specialized high pressure wind tunnel facility, allowing for high Reynolds numbers and low free-stream turbulence levels.

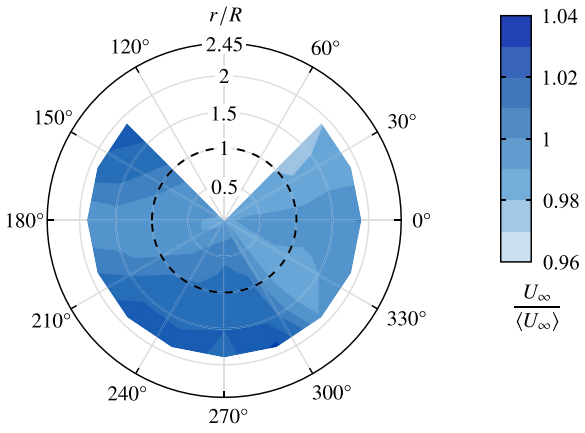

Fig. 1. Free-stream uniformity in the empty test section at $x/D = 0.65$, $Re_D = 4 \times 10^6$. Black dashed circle indicates turbine swept area. Measurements in unshaded region not possible due to traverse limits.

2. Experimental setup

Experiments were conducted in the High Reynolds number Test Facility (HRTF) at Princeton University at a nominal diameter-based Reynolds number of $Re_D = 4 \times 10^6$; achieved at a relatively low flow velocity ($<10\,\mathrm{m\,s^{-1}}$) by using air pressurized up to 238 bar as the working fluid. The facility has a 4.88 m long circular test section with an inner diameter of 49 cm, yielding a 16.7% solid blockage ratio for a 20 cm diameter (D, radius, R) model. Flow conditioning is provided by a honeycomb insert and three turbulence screens, resulting in a free-stream turbulence intensity of 1.2% and an integral length scale of approximately $0.46D$ at $Re_D = 4 \times 10^6$. This and free-stream uniformity were verified via hot-wire anemometry (HWA) measurements in the empty test section, with the latter plotted in Fig. 1, showing uniformity to be within ±3% at a location $0.65D$ downstream from the model.

A sectional view of the HRTF test section is provided in Fig. 2, showing the wind turbine model, its measurement stack, and the cylindrical coordinate system (r, θ, x), with its origin located at the turbine hub. The model turbine rotor is a self-starting, three-bladed design by Miller et al. (2019), with a 20 cm diameter and a total solidity of 18.2%. Throughout, total solidity is calculated as the projection of a model's solid area over the rotor swept area. The turbine measurement stack consists of a six-axis load cell (JR3 Inc. *75E20A4*) with a load rating of 200 N and a total accuracy of ±0.5 N, and a torque transducer (Magtrol *TM-305*) with a 2 N m range and rated accuracy of ±0.003 N m. Together, these provide measurements of the generated streamwise thrust force, F_x, torque, τ, and rotational speed, ω. The measured thrust force is used to determine the thrust coefficient,

$$C_T = \frac{F_x}{\frac{1}{2}\rho {U_\infty}^2 \pi R^2},$$

where ρ is the fluid density and U_∞ is the free-stream velocity. Control over the rotor rotational speed is provided by a magnetic hysteresis

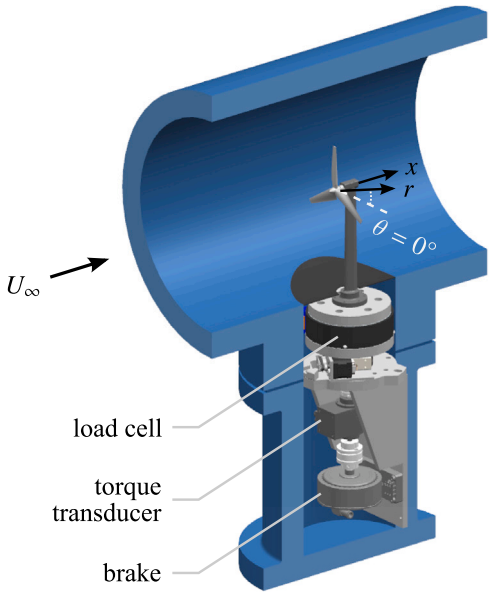

Fig. 2. Sectional view of HRTF test section showing turbine model and measurement stack.

brake (Magtrol *AHB-3*), thus allowing for control of the rotor tip-speed ratio, $\lambda = \omega R/U_\infty$, independent of the free-stream velocity and hence Reynolds number. Further details on the experimental setup and model turbine, including full performance and wake characterizations are available in Miller et al. (2019) and Piqué et al. (2022b).

Ambient temperature and static pressure in the test section are measured via a resistance temperature detector (Omega *PR-10*, ±0.20 °C accuracy) and a pressure transducer (Omega *PX419*, 240 bar range, ±0.08% accuracy), respectively. Determination of fluid density and dynamic viscosity, μ, are available from these measurements using the method outlined by Smits and Zagarola (2005), resulting in uncertainties of ±0.4% and ±0.8% for ρ and μ, respectively. The free-stream velocity is measured 3.8D upstream of the model via a pitot-static tube connected to a Validyne *DP15* differential pressure transducer (13.8 kPa range, ±69 Pa accuracy). Thus, the total uncertainty on $Re_D = 4 \times 10^6$ is ±5%.

Velocity measurements in the turbine wake are measured via HWA in radial, r, scans at various azimuthal, θ, and streamwise, x, positions. A nano-scale thermal anemometry probe (NSTAP, Bailey et al., 2010) with a sensing element size of 60 × 2 × 0.100 μm was used in combination with a Dantec *StreamLine Pro* constant temperature anemometer bridge, with the bridge output digitized by a 16-bit National Instruments *PCI 6123* data acquisition module. Probe positioning was controlled by a three-axis traverse system mounted inside the test section, with the uncertainty in positioning less than ±0.25 mm (r and x) and ±0.25° (θ). Sampling was performed at 200 kHz for a total of 10.5 s, thus collecting 2^{21} samples per measurement location. A wait period of 2 s was used between traverse moves to ensure movement related vibrations had sufficiently decayed. Calibration was performed *in-situ*, with the HWA sensor and a reference pitot-static tube both located in the free-stream, with the latter connected to a Validyne *DP15* pressure transducer (3.45 kPa range, ±19 Pa accuracy). Calibration was performed whenever the working fluid temperature changed by more than 1 °C, using 15 calibration points spanning between $0 \leq U/U_\infty \leq 2$ with a fourth order polynomial fit to the voltage response. The uncertainty in the HWA measurements is estimated to be less than 4.5% within the velocity range $0.55 \leq U/U_\infty \leq 2$, while higher uncertainties are present in the turbine near wake ($x/D \leq 2$), where the velocity deficit is the highest.

Table 1
Rotor and disk parameters, $Re_D = 4 \times 10^6$. C_T corrected for blockage using the method of Bahaj et al. (2007). Length scale of disk openings, ℓ, given as ratio to rotor tip chord length, c_{tip} = 11.1 mm.

	Total solidity	C_T	ℓ
Rotor, $\lambda = 5$	0.182	0.76 ± 4.1%	–
Rotor, $\lambda = 7$		0.68 ± 4.6%	
UD	0.428	0.69 ± 2.9%	0.57
ND1	0.414	0.76 ± 2.5%	0.13–2.77
ND2	0.414	0.69 ± 4.0%	0.13–1.14

3. Porous disk design

As mentioned in Section 1, previous porous disks studies used iterative tuning to obtain similar wakes between disks and turbines. To reduce the iterative design process, a goal of this study is to determine if integrating turbine geometric characteristics into porous disks can improve the agreement between disk and turbine wakes. Therefore, with a given turbine geometry, a more economical and simpler turbine-specific porous/actuator disk could be deployed in wind tunnel tests or simulations. In this section, such a design process is described, where a new style of porous disk is introduced that matches the investigated HAWT rotor in terms of three design criteria: (i) thrust coefficient, (ii) radial solidity distribution, and (iii) length scales.

In total, three porous disk designs are considered, shown in Fig. 3; one with a uniform solidity distribution (UD), and two with non-uniform distributions (ND1 and ND2). ND2 incorporates all three design criteria, while ND1 and UD intentionally lack specific features (length scale and radial solidity distribution matching, respectively) in hopes of isolating the effect of each feature in the wake characterizations that follow in Section 4. Key disk and rotor parameters are summarized in Table 1. All disks match the rotor in diameter, D = 20 cm, and were fabricated from steel to a finished thickness of 7 mm. Finite element analysis results confirm deflection at the disks' edges to be less than 0.1 mm under typical loading conditions (15 N of thrust at $Re_D = 4 \times 10^6$). The UD and ND2 designs include a 1 mm thick layer of woven stainless steel mesh; clamped between 3 mm thick front and back pieces. Design files of the disks are available at Appendix A.

The uniform disk is included as a point of reference to several previous studies which have used similar designs (*e.g.*, Lignarolo et al., 2014; Aubrun et al., 2019). Its total solidity is 42.8%, selected to match the rotor's thrust coefficient at $\lambda = 7$ and $Re_D = 4 \times 10^6$, as per Table 1. The layer of woven wire mesh has an opening size of 6.35 mm, making the predominant length scale of the disk's openings $\ell = 0.57 c_{tip}$, where c_{tip} = 11.1 mm and is the rotor tip chord length.

Disks ND1 and ND2 feature non-uniform solidity distributions, plotted in Fig. 4, designed to mimic the radial solidity distribution of the rotor. The disks are designed in six annular segments (marked by the vertical dotted lines in Fig. 4), where within each segment, the disk solidities are set equal to the average solidity of the rotor plus a positive offset (indicated by the colored labels in Fig. 4). The offsets vary from 0 to 25% from the inner to outermost segments, and are required to increase the total solidity of each disk to 41.4% in order to match the thrust coefficient of the rotor. ND1 and ND2 differ in their predominant length scales, as ℓ varies from $0.1 c_{tip}$ near the center for both disks, to $2.77 c_{tip}$ and $1.14 c_{tip}$ near the edge, for ND1 and ND2 respectively. Ideally, the radial solidity distributions of ND1 and ND2 would be identical, however adding the mesh layer to ND2 required slight modifications to its radial solidity distribution to preserve structural rigidity. That said, both disks have total solidities of 41.4% and radial solidity distributions that approximate the rotor profile reasonably well, as per Fig. 4. From Table 1, ND2 yields a thrust coefficient that matches the rotor at $\lambda = 7$ and UD, however, a higher thrust coefficient is found for ND1 which matches the rotor at $\lambda = 5$, with the difference in thrust likely stemming from different wake shedding characteristics (Steiros and Hultmark, 2018).

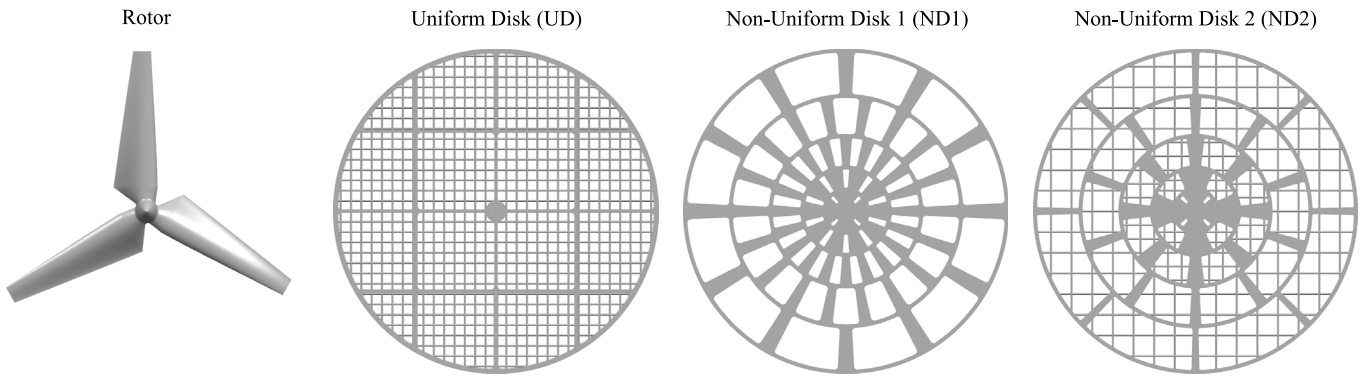

Fig. 3. Rotor and investigated porous disks. Rotor details are available in Miller et al. (2019). Disk design files are available at Appendix A.

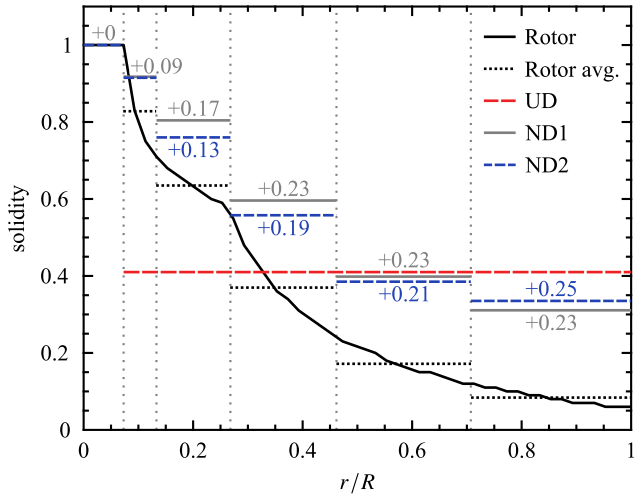

Fig. 4. Radial solidity distributions of the rotor and porous disks. Rotor avg., ND1 and ND2 solidities are averages within the annular segments marked by the gray dotted lines. Labels (colored according to legend) indicate offsets applied to rotor averages to give ND1 and ND2 solidities.

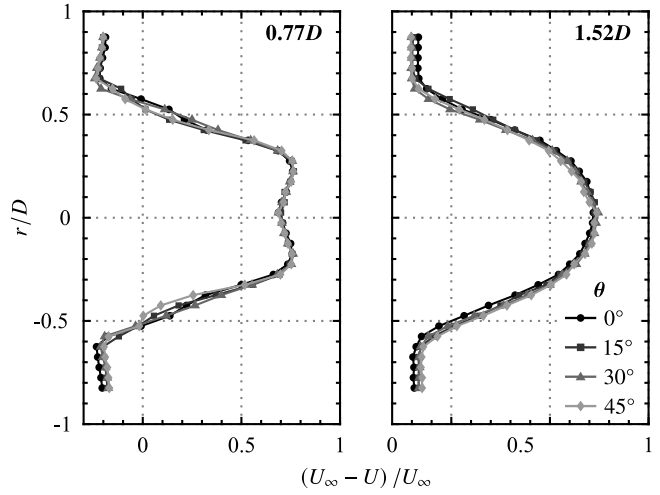

Fig. 5. Effect of azimuthal angle on near wake mean velocity deficit for ND1. Bold labels indicate streamwise position.

Prior to comparing the rotor and disk results it is important to establish any axial asymmetry that may be present in the disk wakes, since none of the porous disks designs are axisymmetric. This is examined in Fig. 5, where the mean velocity deficit, $(U_\infty - U)/U_\infty$, of ND1 is plotted for several azimuthal angles at two streamwise positions in the near wake. From Fig. 5, a minor effect on azimuthal angle is seen at $x/D = 0.77$ as the curves show slight discrepancies near the disk edge, $r/D = \pm 0.5$. However, this dependence is no longer present at the following downstream station, $x/D = 1.52$, where the curves show near perfect collapse. Disks UD and ND2 show similar results (not shown for brevity), and thus for all models investigated the flow is assumed radially axisymmetric, with all following wake profiles measured at $\theta = 0°$.

4. Wake comparisons

In this section the proposed design improvements to the porous disk model are evaluated through comparisons of mean velocity and turbulent statistics in the wakes of a model HAWT and the three porous disks (UD, ND1 and ND2, see Fig. 3). All comparisons are made at a diameter-based Reynolds number of $Re_D = 4 \times 10^6$ and with free-stream turbulence intensity of 1.2%. Rotor tip-speed ratios of $\lambda = 5$ and 7 are considered as these yield thrust coefficients that match the ND1, and UD and ND2 disks, respectively (refer to Table 1). Throughout the discussion, the distinction between the near and intermediate wake is taken at $x/D = 3$, as established for this turbine by Piqué et al. (2022b).

Fig. 6 presents the wake development of the turbine and disks in terms of the mean streamwise velocity deficit, with the results of ND1 plotted separately from UD and ND2 in order to ease comparisons with the proper rotor cases. Beginning with the rotor results, the mean velocity deficit profiles show typical HAWT wake development, with a relatively narrow wake with a high velocity deficit in the near wake ($x/D \leq 3$) that widens and recovers toward the free-stream velocity with downstream development. Significant blockage effects are present, as the maximum velocity outside the wake is approximately $1.2U_\infty$. This is to be expected given the 16.7% solid blockage ratio, however, it is of no major concern as the interest here is the comparison between the rotor and disk wakes, all of which are subject to the same blockage.

Comparing the ND1 results with the rotor at $\lambda = 5$, as expected, the agreement is rather poor at the two most upstream stations ($x/D = 0.77$ and 1.02), as the disk wake is significantly wider, however, the agreement improves significantly at the following two stations, with a near perfect match at $x/D = 2.02D$. However, this is still within the near wake region, where the rotor wake has yet to attain self-similarity. Based on the findings of Aubrun et al. (2013), matching the wake here does not guarantee a continued match with downstream development. This is indeed the case, as the ND1 wake recovers more rapidly than that of the rotor, leading to differences of up to 18% and 30% in maximum velocity deficit at $x/D = 3.52$ and 6.52, respectively, and overall poor agreement. The result indicates that the ND1 wake is subject to stronger turbulent diffusion, which must be driven by the turbulence in the wake and not solely by the ambient free-stream turbulence level, since the latter is equal for the rotor and ND1 cases.

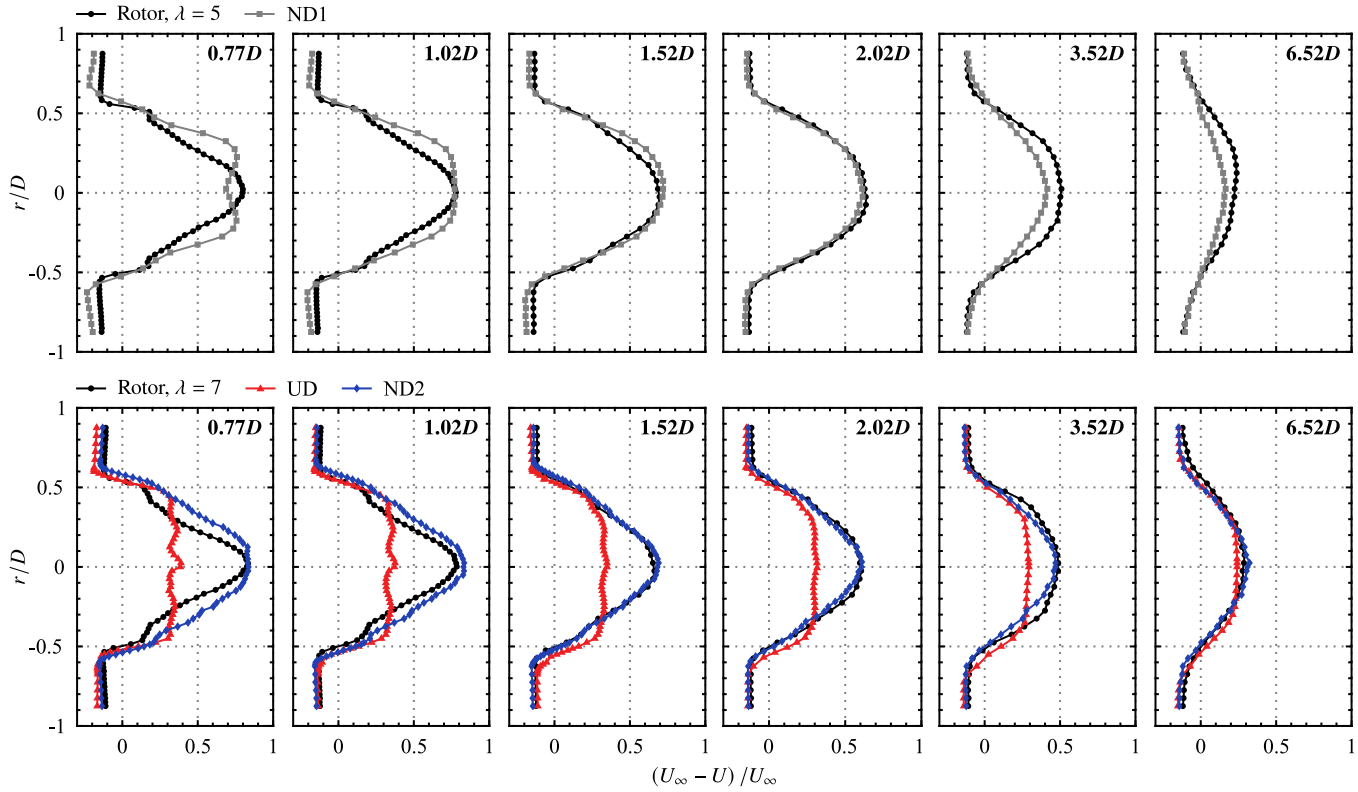

Fig. 6. Wake profiles of mean streamwise velocity deficit. Bold labels indicate streamwise position.

The stark differences between the UD and ND2 profiles presented in Fig. 6 highlight the significant effects of radial solidity distribution on the development of mean velocity in a porous disk wake. The uniform porous disk creates a strong 'top hat'-like mean velocity profile, with a flat velocity deficit between the disk edges ($r/D = \pm 0.5$) whose centerline magnitude is significantly less than that of the rotor in the near wake. The UD velocity deficit recovers much slower than the rotor wake, increasing by only $0.14U_\infty$ at the wake centerline between $x/D = 0.77$ and 6.52 (compared to $0.55U_\infty$ for the rotor), eventually matching the rotor profile at the farthest downstream station. Overall, the performance of the uniform porous disk is rather poor, especially when compared to ND2, which shows a near perfect match to the rotor that begins at $x/D = 1.02$ and extends throughout the entire measured wake.

The results from Fig. 6 make it clear that, as a single design criterion, matching the rotor thrust coefficient is insufficient for porous and actuator disk design, as each of the presented disks are matched in this regard (Table 1) and yet reproduce the rotor mean wakes to varying degrees of success. By comparing UD to ND1 and ND2, it is clear disks should be designed with a radial solidity distribution that is similar to that of the rotor (Fig. 4), as this significantly improves mean velocity profile agreement in both the near and intermediate wakes. That is not to say that a uniform porous or actuator disk cannot serve as an accurate wind turbine model, as Aubrun et al. (2013) and Lignarolo et al. (2014) demonstrate this. Rather, the solidity distribution of a disk should be considered in order to achieve desired wake characteristics, with the radial solidity distribution of the rotor serving as a convenient design criterion (*i.e.*, known *a priori*) that yields acceptable levels of accuracy.

While both ND1 and ND2 outperform UD in terms of matching the rotor velocity profiles in Fig. 6, differences between ND1 and ND2 are apparent, most notably in the intermediate wake ($x/D = 3.52$ and 6.52), which are likely related to the turbulence generated in the wake. This is examined in Fig. 7, where profiles of the root-mean-square of streamwise velocity fluctuations, u'_{rms}, are plotted. Examining ND1 and its corresponding rotor case ($\lambda = 5$), the expected peaks in the near wake at $r/D = \pm 0.5$ are seen in the rotor profile and correspond to the tip vortices. For ND1, a double peak structure is present (peaks at $r/D = \pm 0.6$ and ± 0.4, most notable at $x/D = 0.77$), which likely correspond to an annular shear layer shed from the disk edge and large coherent structures that are shed from the large openings at the disk edge, respectively. Moving downstream, these two peaks collapse to form a distribution that matches the shape of the rotor profile in the intermediate wake ($x/D = 3.52$ and 6.52), however, the amplitude of the fluctuations remains significantly higher (*e.g.*, peak amplitudes 1.5 and 1.3 times higher at $x/D = 3.52$ and 6.52, respectively). As postulated earlier, the faster wake recovery of ND1 is indeed driven by the turbulent structures generated within the wake, as the relatively large openings in ND1 shed large, energetic structures, yielding larger integral length scales and more turbulent kinetic energy which dominate the wake and its recovery process. This will be explored further through spectral analysis of the velocity fluctuations that follows later in this section.

The added layer of mesh to ND2 reduces the size of the openings at the disk edge to the order of the rotor's tip chord length (Table 1), presumably resulting in reduced integral length scales introduced into the flow. These effects are explored through comparison of the ND1 and ND2 results in Fig. 7. At $x/D = 0.77$, the inner peak of ND1 at $r/D = \pm 0.4$ is shifted further inward and is reduced in magnitude significantly by the mesh layer of ND2, indicating that the inner wake of ND2 consists of smaller, less energetic structures. Overall, the result of ND2 better approximate the rotor's profile of turbulent fluctuations in the near wake ($x/D < 3$), with agreement improving into the intermediate wake, as turbulence from the disk shear layer and inner wake shedding diffuse to form a profile that is well matched to the rotor at $x/D = 3.52$ and 6.52. By comparison, fluctuations in the UD far wake are of a similar profile but are significantly lower in amplitude, having decayed from levels that matched the rotor in the near wake.

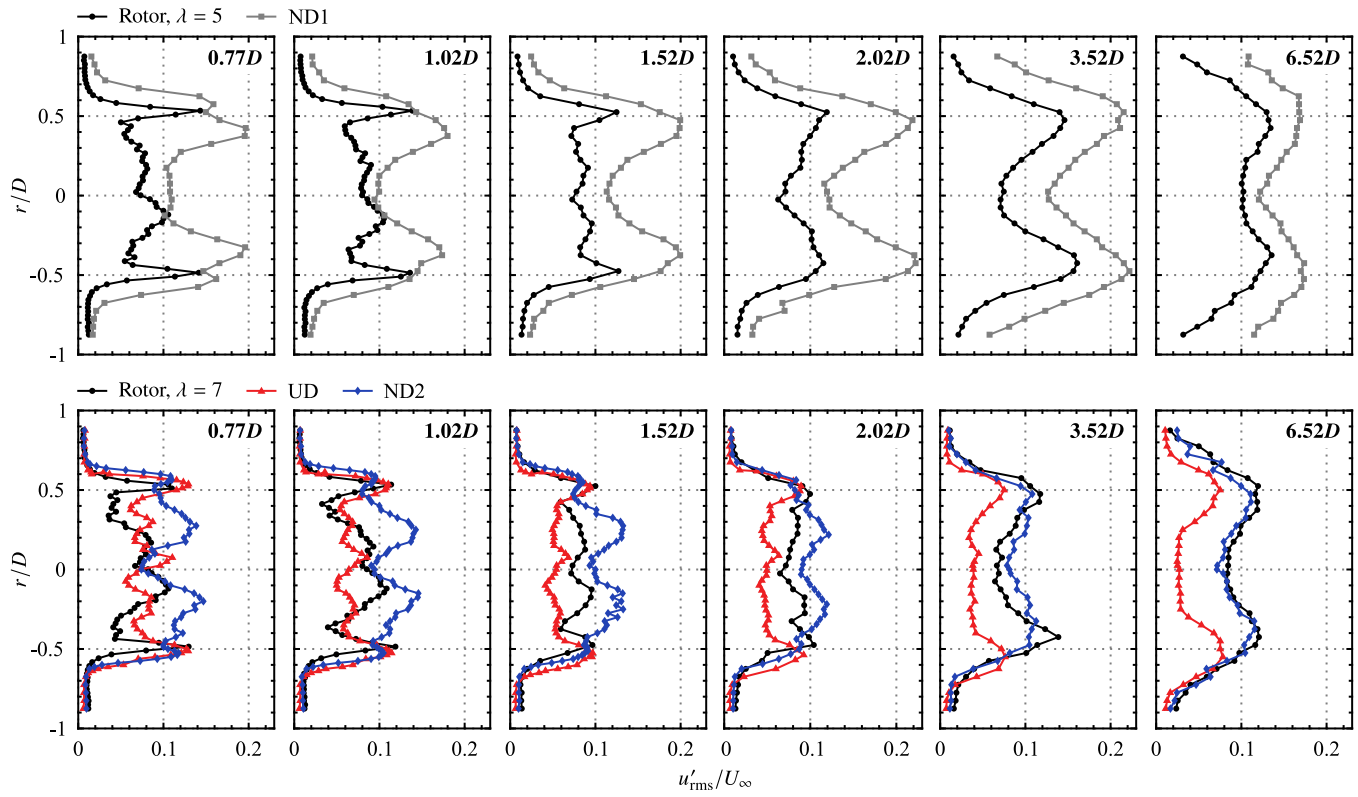

Fig. 7. Wake profiles of the root-mean-square of streamwise velocity fluctuations. Bold labels indicate streamwise position.

The results of Fig. 7 highlight the important interplay between free-stream and wake generated turbulence, and its influence on the performance of the porous disk as a wind turbine model. In other wind tunnel studies, where Reynolds numbers are low and atmospheric boundary layer conditions are replicated (*e.g.*, Aubrun et al., 2013; Camp and Cal, 2016, 2019), the high levels of free-stream turbulence tend to dominate the wake development, causing a rapid diffusion of turbulence in the near wake that leads to agreement between porous disk and turbines in the intermediate wake (*e.g.*, see Fig. 9 in Aubrun et al., 2013). Here, and in Vinnes et al. (2022), the low levels of free-stream turbulence limit diffusion by the ambient turbulence, and so turbulence generated by the model has a strong and lasting influence on wake development. Thus, for a porous disk to provide an accurate wake model in such conditions, it is imperative that the disk itself generate turbulence of similar characteristics (*i.e.*, amplitude and spatial distribution) to that of the rotor. As demonstrated by ND2 (Fig. 7), this can be achieved by incorporating physical features into the disk that match the length scales of the rotor, with the rotor tip chord length proving to be an effective choice.

Higher order velocity statistics are an important consideration as previous results have shown these are particularly sensitive to position within the wake (Camp and Cal, 2016), the type of disk (Vinnes et al., 2022), and the free-stream turbulence level (Aubrun et al., 2013). This is examined in the present study via streamwise velocity skewness, S_u, plotted in Fig. 8. In the free-stream, where the turbulence is approximately isotropic, a skewness of zero is expected, while non-zero values are expected in regions of strong mean velocity gradients. This is indeed the case in the near wake ($x/D = 1.02$), as the skewness varies significantly within $-0.7 < r/D < 0.7$ and the trends between all disks and the respective rotor cases differ significantly. Moving into the intermediate wake, where the wake turbulence has diffused and decayed, the agreement improves, most notably for the ND2 case as the skewness profiles match relatively well at both $x/D = 3.52$ and 6.52. These results further support ND2 as a suitable turbine model for high Reynolds numbers and low free-stream turbulence conditions, as

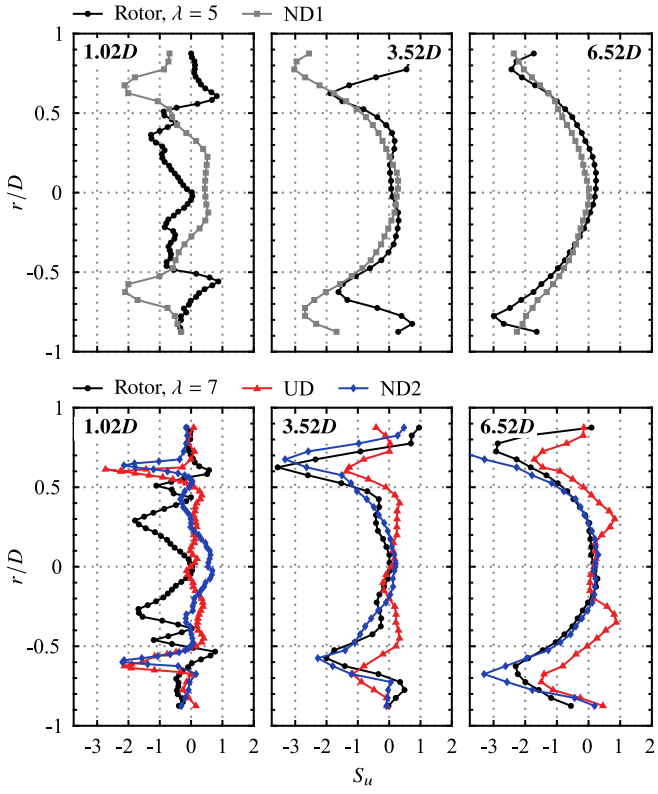

Fig. 8. Wake profiles of streamwise velocity skewness. Bold labels indicate streamwise position.

turbulent statistics, verified up to the second and third moments, are well matched in the intermediate wake (Figs. 7 and 8).

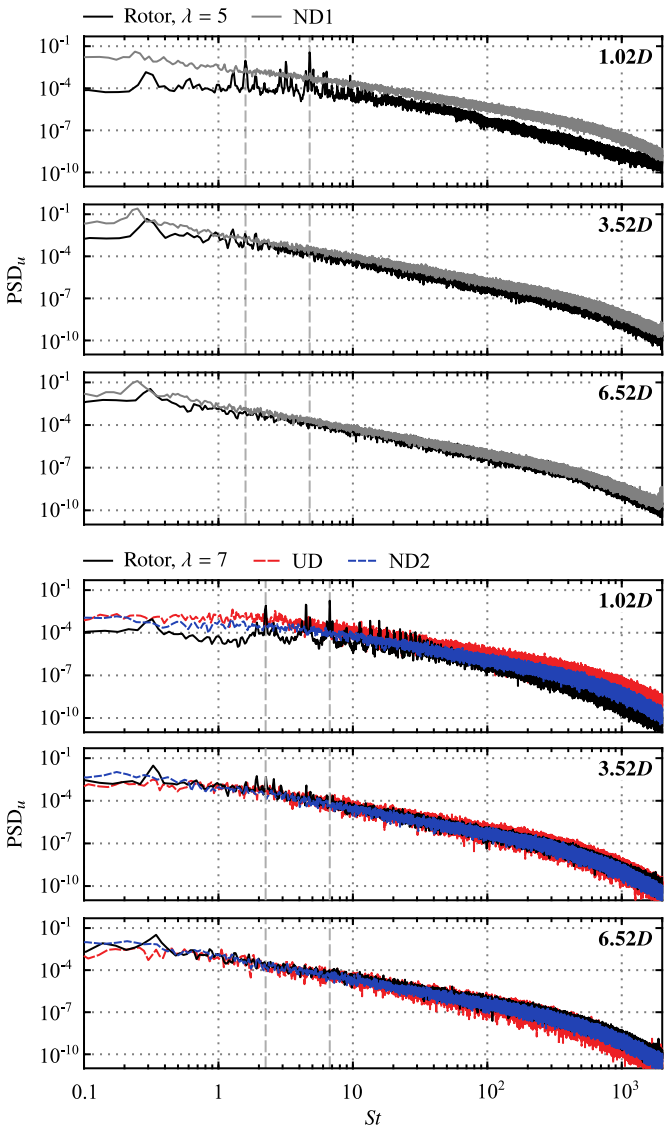

Fig. 9. Power spectral density of streamwise velocity at $r/D = 0.5$. Gray dashed lines mark one and three times the rotor's rotational frequency. Bold labels indicate streamwise position.

The frequency content of the fluctuations present within the wakes at $r/D = 0.5$ are compared via the power spectral density of the streamwise velocity, PSD_u, in Fig. 9. Frequency, f, is non-dimensionalized into a Strouhal number based on the free-stream convective time scale, $St = fD/U_\infty$, and the spectra are calculated using the Welch method (Welch, 1967) by dividing signals into 7 windows, overlapped by 50% and each containing 2^{19} samples, resulting in a non-dimensional frequency resolution of 0.035. The rotational frequencies of the rotor ($St_0 = 1.60$ and 2.25 for $\lambda = 5$ and 7, respectively) and three times these values are indicated in Fig. 9 by the gray dashed lines. In the near wake ($x/D = 1.02$), the rotor cases show signatures of the turbine rotation and passage of the three blades, each creating a tip vortex, with strong peaks found at St_0 and $3St_0$. As expected, no such activity is seen in the spectra of the porous disks.

In Fig. 9, the ND1 spectra show significantly higher fluctuating amplitudes across all frequencies, but in particularly for $St < 1$. High spectral amplitudes at low frequencies indicates the presence of large coherent structures containing a significant portion of the turbulent kinetic energy budget, whose presence were also postulated in examining the elevated levels of u'_{rms} in the near wake (Fig. 7) and the accelerated mean velocity recovery in the far wake (Fig. 6). In contrast, UD and ND2 show reduced levels within $St < 1$ compared to ND1, indicating that their layers of added mesh are effective at mitigating the shedding of large, energetic structures, resulting in spectra that, while still elevated at low frequencies and missing rotational signatures, are more representative of the rotor spectrum at $x/D = 1.02D$. The rotational signatures have decayed substantially by $x/D = 3.52$ and are all but gone by $x/D = 6.52$, indicating the transition into the intermediate wake. As has been seen across all other metrics (Figs. 6 to 8), it is here where the best agreement is found between the porous disks and rotor, with the ND2 disk and rotor spectra showing excellent agreement across the entire measured frequency range in Fig. 9.

5. Conclusions

A new design methodology for porous disk wind turbine modeling was proposed and experimentally tested. The approach involves matching a porous disk to a horizontal axis wind turbine based on its (i) thrust coefficient, (ii) radial solidity distribution, and (iii) length scales, all of which do not require *a priori* knowledge of wake characteristics. Three porous disk designs were considered, with all three criteria incorporated into one design, while the effects of criteria (ii) and (iii) were explored through their omission from the other two disk designs. Performance was evaluated through wake comparisons with a model HAWT at a diameter-based Reynolds number of 4×10^6 and a free-stream turbulence intensity of 1.2%, since these conditions are predicted to be the most challenging for accurate porous disk HAWT modeling, had yet to be tested in the literature, and are relevant to offshore wind turbine operation.

Wake velocity measurements were performed via nano-scale HWA in a pressurized wind tunnel facility, revealing that incorporating the radial solidity distribution of the rotor into the design of the porous disk can yield excellent agreement on mean streamwise velocity deficit profiles in the near wake (streamwise distance as early as $x/D = 1.5$). This agreement can persist throughout the wake, however, in a high Reynolds number, low free-stream turbulence environment, diffusion by the ambient turbulence is limited and therefore the turbulence generated within the wake dominates its own development and recovery process. Therefore, for an accurate porous disk model, the disk must inject turbulence into the near wake with similar characteristics (*i.e.*, amplitude and distribution) to that of the rotor. This is achieved through the third design criterion, where physical features that match the length scales of the rotor are incorporated, with the rotor tip chord length proving to be an effective target length scale. However, a stationary porous disk cannot recreate the rotational wake dynamics generated by the rotor, and therefore agreement on higher order velocity statistics is only found once the wake has transitioned into the intermediate region; occurring at a downstream streamwise distance of approximately three and a half rotor diameters.

In summary, incorporating all three design criteria into a single porous disk yields a HAWT model that performs well at high Reynolds numbers and low free-stream turbulence intensities; offering accurate modeling of mean velocity and higher order statistics in the intermediate wake, with the former also showing good agreement in the near wake. These results carry important implications for the actuator disk model in high Reynolds numbers and/or low free-stream turbulence intensities flows. As an example, a simpler model that only adheres to the first design criterion can yield accurate results if the free-stream turbulence intensity is 'high enough', however, such a determination is arbitrary and, in the authors' opinion, should be avoided by using the design approach developed herein.

CRediT authorship contribution statement

John W. Kurelek: Conceptualization, Methodology, Investigation, Formal analysis, Writing – original draft. **Alexander Piqué:** Conceptualization, Investigation, Writing – review & editing. **Marcus Hultmark:** Conceptualization, Supervision, Writing – review & editing.

Declaration of competing interest

The authors declare that they have no known competing financial interests or personal relationships that could have appeared to influence the work reported in this paper.

Data availability

Design files for the porous disks are available at https://doi.org/10.1016/j.jweia.2023.105377. All other data available upon request.

Acknowledgments

The authors gratefully acknowledge funding support from the Natural Sciences and Engineering Research Council of Canada and the National Science Foundation, USA under Grant No. CBET 1652583 (Program Manager Ron Joslin).

Appendix A. Supplementary data

Supplementary material related to this article can be found online at https://doi.org/10.1016/j.jweia.2023.105377.

References

Aubrun, S., Bastankhah, M., Cal, R.B., Conan, B., Hearst, R.J., Hoek, D., Hölling, M., Huang, M., Hur, C., Karlsen, B., Neunaber, I., Obligado, M., Peinke, J., Percin, M., Saetran, L., Schito, P., Schliffke, B., Sims-Williams, D., Uzol, O., Vinnes, M.K., Zasso, A., 2019. Round-robin tests of porous disc models. J. Phys. Conf. Ser. 1256 (1), http://dx.doi.org/10.1088/1742-6596/1256/1/012004.

Aubrun, S., Loyer, S., Hancock, P., Hayden, P., 2013. Wind turbine wake properties: Comparison between a non-rotating simplified wind turbine model and a rotating model. J. Wind Eng. Ind. Aerodyn. 120, 1–8. http://dx.doi.org/10.1016/j.jweia.2013.06.007.

Bahaj, A., Molland, A., Chaplin, J., Batten, W., 2007. Power and thrust measurements of marine current turbines under various hydrodynamic flow conditions in a cavitation tunnel and a towing tank. Renew. Energy 32 (3), 407–426. http://dx.doi.org/10.1016/j.renene.2006.01.012.

Bailey, S.C.C., Kunkel, G.J., Hultmark, M., Vallikivi, M., Hill, J.P., Meyer, K.A., Tsay, C., Arnold, C.B., Smits, A.J., 2010. Turbulence measurements using a nanoscale thermal anemometry probe. J. Fluid Mech. 663, 160–179. http://dx.doi.org/10.1017/S0022112010003447.

Barthelmie, R.J., Frandsen, S.T., Nielsen, M.N., Pryor, S.C., Rethore, P.-E., Jørgensen, H.E., 2007. Modelling and measurements of power losses and turbulence intensity in wind turbine wakes at middelgrunden offshore wind farm. Wind Energy 10 (6), 517–528. http://dx.doi.org/10.1002/we.238.

Barthelmie, R., Hansen, O.F., Enevoldsen, K., Højstrup, J., Frandsen, S., Pryor, S., Larsen, S., Motta, M., Sanderhoff, P., 2005. Ten years of meteorological measurements for offshore wind farms. J. Sol. Energy Eng. 127 (2), 170–176. http://dx.doi.org/10.1115/1.1850489.

Barthelmie, R.J., Pryor, S.C., Frandsen, S.T., Hansen, K.S., Schepers, J.G., Rados, K., Schlez, W., Neubert, A., Jensen, L.E., Neckelmann, S., 2010. Quantifying the impact of wind turbine wakes on power output at offshore wind farms. J. Atmos. Ocean. Technol. 27 (8), 1302–1317. http://dx.doi.org/10.1175/2010JTECHA1398.1.

Blackmore, T., Batten, W.M.J., Müller, G.U., Bahaj, A.S., 2014. Influence of turbulence on the drag of solid discs and turbine simulators in a water current. Exp. Fluids 55 (1), 1637. http://dx.doi.org/10.1007/s00348-013-1637-9.

Bossuyt, J., Howland, M.F., Meneveau, C., Meyers, J., 2017. Measurement of unsteady loading and power output variability in a micro wind farm model in a wind tunnel. Exp. Fluids 58 (1), 1. http://dx.doi.org/10.1007/s00348-016-2278-6.

Calaf, M., Meneveau, C., Meyers, J., 2010. Large eddy simulation study of fully developed wind-turbine array boundary layers. Phys. Fluids 22 (1), 015110. http://dx.doi.org/10.1063/1.3291077.

Camp, E.H., Cal, R.B., 2016. Mean kinetic energy transport and event classification in a model wind turbine array versus an array of porous disks: Energy budget and octant analysis. Phys. Rev. Fluids 1 (4), 044404. http://dx.doi.org/10.1103/PhysRevFluids.1.044404.

Camp, E.H., Cal, R.B., 2019. Low-dimensional representations and anisotropy of model rotor versus porous disk wind turbine arrays. Phys. Rev. Fluids 4 (2), 024610. http://dx.doi.org/10.1103/PhysRevFluids.4.024610.

Chamorro, L.P., Arndt, R.E.A., Sotiropoulos, F., 2012. Reynolds number dependence of turbulence statistics in the wake of wind turbines. Wind Energy 15 (5), 733–742. http://dx.doi.org/10.1002/we.501.

Chamorro, L.P., Porté-Agel, F., 2009. A wind-tunnel investigation of wind-turbine wakes: Boundary-layer turbulence effects. Bound.-Layer Meteorol. 132 (1), 129–149. http://dx.doi.org/10.1007/s10546-009-9380-8.

Dahlberg, J.Å., Thor, S.E., 2009. Power performance and wake effects in the closely spaced lillgrund wind farm. In: Proc. Eur. Offshore Wind 2009 Conf. Exhib.. Stockholm SE, Sept 14–16.

De Rijcke, S., Driesen, J., Meyers, J., 2015. Power smoothing in large wind farms using optimal control of rotating kinetic energy reserves. Wind Energy 18 (10), 1777–1791. http://dx.doi.org/10.1002/we.1790.

España, G., Aubrun, S., Loyer, S., Devinant, P., 2011. Spatial study of the wake meandering using modelled wind turbines in a wind tunnel. Wind Energy 14 (7), 923–937. http://dx.doi.org/10.1002/we.515.

Goit, J.P., Meyers, J., 2015. Optimal control of energy extraction in wind-farm boundary layers. J. Fluid Mech. 768, 5–50. http://dx.doi.org/10.1017/jfm.2015.70.

GWEC, 2021. Global Wind Report 2021. Global Wind Energy Council, p. 80, URL: http://www.gwec.net/global-figures/wind-energy-global-status/.

Hansen, M.O.L., 2008. Aerodynamics of Wind Turbines, second ed. Earthscan.

Hansen, K.S., Barthelmie, R.J., Jensen, L.E., Sommer, A., 2012. The impact of turbulence intensity and atmospheric stability on power deficits due to wind turbine wakes at horns rev wind farm. Wind Energy 15 (1), 183–196. http://dx.doi.org/10.1002/we.512.

Hattori, Y., Yamamoto, M., Eguchi, Y., Kondo, K., Suto, H., Tanaka, N., 2007. A wind tunnel experiment on wake structure of a wind turbine. In: Eur. Wind Energy Conf. Exhib. 2007. WindEurope, Milan, IT, http://dx.doi.org/10.13140/2.1.5141.0727, May 7–10.

Helvig, S.d.J., Vinnes, M.K., Segalini, A., Worth, N.A., Hearst, R.J., 2021. A comparison of lab-scale free rotating wind turbines and actuator disks. J. Wind Eng. Ind. Aerodyn. 209 (June 2020), 104485. http://dx.doi.org/10.1016/j.jweia.2020.104485.

Higuchi, H., Zhang, J., Muzas, B., Furuya, S., Higuchi, H., Zhang, J., Muzas, B., Furuya, S., 1997. Experimental study on unsteady flows and multiple near-wake patterns behind slotted disks. In: 14th Aerodyn. Decelerator Syst. Technol. Conf.. American Institute of Aeronautics and Astronautics, San Francisco CA, Jun 3–5, pp. 214–224. http://dx.doi.org/10.2514/6.1997-1480, URL: https://arc.aiaa.org/doi/10.2514/6.1997-1480.

IRENA, 2020. Global Renewables Outlook: Energy Transformation 2050. International Renewable Energy Agency, p. 292, URL: https://www.irena.org/publications/2020/Apr/Global-Renewables-Outlook-2020.

Krogstad, P.-Å., Adaramola, M.S., 2012. Performance and near wake measurements of a model horizontal axis wind turbine. Wind Energy 15 (5), 743–756. http://dx.doi.org/10.1002/we.502.

Lebron, J., Castillo, L., Meneveau, C., 2012. Experimental study of the kinetic energy budget in a wind turbine streamtube. J. Turbul. 13, N43. http://dx.doi.org/10.1080/14685248.2012.705005.

Li, L., Hearst, R., Ferreira, M., Ganapathisubramani, B., 2020. The near-field of a lab-scale wind turbine in tailored turbulent shear flows. Renew. Energy 149, 735–748. http://dx.doi.org/10.1016/j.renene.2019.12.049.

Lignarolo, L.E.M., Ragni, D., Ferreira, C.J.S., van Bussel, G.J.W., 2014. Kinetic energy entrainment in wind turbine and actuator disc wakes: an experimental analysis. J. Phys. Conf. Ser. 524 (1), 012163. http://dx.doi.org/10.1088/1742-6596/524/1/012163.

Markfort, C.D., Zhang, W., Porté-Agel, F., 2012. Turbulent flow and scalar transport through and over aligned and staggered wind farms. J. Turbul. 13, N33. http://dx.doi.org/10.1080/14685248.2012.709635.

Medici, D., Alfredsson, P.H., 2006. Measurements on a wind turbine wake: 3D effects and bluff body vortex shedding. Wind Energy 9 (3), 219–236. http://dx.doi.org/10.1002/we.156.

Mehta, D., van Zuijlen, A., Koren, B., Holierhoek, J., Bijl, H., 2014. Large eddy simulation of wind farm aerodynamics: A review. J. Wind Eng. Ind. Aerodyn. 133, 1–17. http://dx.doi.org/10.1016/j.jweia.2014.07.002.

Meyers, J., Meneveau, C., 2012. Optimal turbine spacing in fully developed wind farm boundary layers. Wind Energy 15 (2), 305–317. http://dx.doi.org/10.1002/we.469.

Miller, M.A., Kiefer, J., Westergaard, C., Hansen, M.O.L., Hultmark, M., 2019. Horizontal axis wind turbine testing at high Reynolds numbers. Phys. Rev. Fluids 4 (11), 110504. http://dx.doi.org/10.1103/PhysRevFluids.4.110504, arXiv:PhysRevFluids.4.110504.

Myers, L.E., Bahaj, A.S., 2010. Experimental analysis of the flow field around horizontal axis tidal turbines by use of scale mesh disk rotor simulators. Ocean Eng. 37 (2–3), 218–227. http://dx.doi.org/10.1016/j.oceaneng.2009.11.004.

Newman, J., Lebron, J., Meneveau, C., Castillo, L., 2013. Streamwise development of the wind turbine boundary layer over a model wind turbine array. Phys. Fluids 25 (8), 085108. http://dx.doi.org/10.1063/1.4818451.

Piqué, A., Miller, M.A., Hultmark, M., 2022a. Dominant flow features in the wake of a wind turbine at high Reynolds numbers. J. Renew. Sustain. Energy 14 (3), 033304. http://dx.doi.org/10.1063/5.0086746.

Piqué, A., Miller, M.A., Hultmark, M., 2022b. Laboratory investigation of the near and intermediate wake of a wind turbine at very high Reynolds numbers. Exp. Fluids 63 (6), 106. http://dx.doi.org/10.1007/s00348-022-03455-0.

Sanderse, B., Pijl, S., Koren, B., 2011. Review of computational fluid dynamics for wind turbine wake aerodynamics. Wind Energy 14 (7), 799–819. http://dx.doi.org/10.1002/we.458.

Sforza, P.M., Sheerin, P., Smorto, M., 1981. Three-dimensional wakes of simulated wind turbines. AIAA J. 19 (9), 1101–1107. http://dx.doi.org/10.2514/3.60049.

Smits, A.J., Zagarola, M.V., 2005. Applications of dense gases to model testing for aeronautical and hydrodynamic applications. Meas. Sci. Technol. 16 (9), 1710–1715. http://dx.doi.org/10.1088/0957-0233/16/9/002.

Soares-Ramos, E.P.P., de Oliveira-Assis, L., Sarrias-Mena, R., Fernández-Ramírez, L.M., 2020. Current status and future trends of offshore wind power in Europe. Energy 202, 117787. http://dx.doi.org/10.1016/j.energy.2020.117787.

Sørensen, J.N., Shen, W.Z., 2002. Numerical modeling of wind turbine wakes. J. Fluids Eng. 124 (2), 393–399. http://dx.doi.org/10.1115/1.1471361.

Steiros, K., Hultmark, M., 2018. Drag on flat plates of arbitrary porosity. J. Fluid Mech. 853, R3. http://dx.doi.org/10.1017/jfm.2018.621.

Theunissen, R., Housley, P., Allen, C.B., Carey, C., 2015. Experimental verification of computational predictions in power generation variation with layout of offshore wind farms. Wind Energy 18 (10), 1739–1757. http://dx.doi.org/10.1002/we.1788.

Tian, W., Ozbay, A., Hu, H., 2014. Effects of incoming surface wind conditions on the wake characteristics and dynamic wind loads acting on a wind turbine model. Phys. Fluids 26 (12), 125108. http://dx.doi.org/10.1063/1.4904375.

Vermeer, L., Sørensen, J., Crespo, A., 2003. Wind turbine wake aerodynamics. Prog. Aerosp. Sci. 39 (6–7), 467–510. http://dx.doi.org/10.1016/S0376-0421(03)00078-2.

Vinnes, M.K., Gambuzza, S., Ganapathisubramani, B., Hearst, R.J., 2022. The far wake of porous disks and a model wind turbine: Similarities and differences assessed by hot-wire anemometry. J. Renew. Sustain. Energy 14 (2), 023304. http://dx.doi.org/10.1063/5.0074218.

Welch, P., 1967. The use of fast Fourier transform for the estimation of power spectra: A method based on time averaging over short, modified periodograms. IEEE Trans. Audio Electroacoust. 15 (2), 70–73. http://dx.doi.org/10.1109/TAU.1967.1161901.

Wu, Y.-T., Porté-Agel, F., 2011. Large-eddy simulation of wind-turbine wakes: Evaluation of turbine parametrisations. Boundary-Layer Meteorol. 138 (3), 345–366. http://dx.doi.org/10.1007/s10546-010-9569-x.

Yang, X., Kang, S., Sotiropoulos, F., 2012. Computational study and modeling of turbine spacing effects in infinite aligned wind farms. Phys. Fluids 24 (11), 115107. http://dx.doi.org/10.1063/1.4767727.

Zhang, W., Markfort, C.D., Porté-Agel, F., 2012. Near-wake flow structure downwind of a wind turbine in a turbulent boundary layer. Exp. Fluids 52 (5), 1219–1235. http://dx.doi.org/10.1007/s00348-011-1250-8.